INTERNATIONAL JOURNAL FOR NUMERICAL METHODS IN FLUIDS
Int. J. Numer. Meth. Fluids 2008; **58**:91–109
Published online 5 December 2007 in Wiley InterScience (www.interscience.wiley.com). DOI: 10.1002/fld.1681

A non-conforming finite-element method for solving non-hydrostatic free-surface flow problems

D. Y. Le Roux[1,*,†], J. L. Robert[2] and M. Gabbouhy[1]

[1]*Département de Mathématiques et de Statistique, Université Laval, Québec, QC, Canada G1K 7P4*
[2]*Département de Génie Civil, Université Laval, Québec, QC, Canada G1K 7P4*

SUMMARY

In this paper, we develop a two-dimensional vertical numerical model for simulating unsteady free-surface flows, using a non-hydrostatic pressure distribution. A fractional step numerical procedure is employed. The governing differential equations are discretized using the finite-element method. The velocity and salinity fields are approximated using the so-called linear non-conforming P_1^{NC} element, and pressure and free-surface elevation are discretized using linear continuous P_1 approximations. This procedure is very efficient and could also be applied to hydrostatic flow problems. Our numerical scheme is validated by three test cases, namely a deepwater standing wave, the propagation of a solitary wave in a long channel and the density-driven flow. Copyright © 2007 John Wiley & Sons, Ltd.

Received 25 May 2007; Revised 11 October 2007; Accepted 14 October 2007

KEY WORDS: free-surface flow; non-hydrostatic model; non-conforming finite elements; projection method

1. INTRODUCTION

In a number of numerical models (e.g. [1–3]), the hydrostatic pressure assumption has been used to study natural free-surface flows (rivers, lakes, estuaries, oceans, etc.). It assumes that the acceleration and eddy viscosity terms in the momentum equation for the vertical velocity component are much smaller than the gravitational acceleration and can thus be neglected. This assumption is valid in many situations and its use is motivated by the fact that the vertical length scale is much smaller than the horizontal one. However, it is well known that the hydrostatic assumption is not valid in the cases of short waves, stratification induced by strong horizontal density gradient, and flows over abruptly changed bottom topography. In such cases, the effects

*Correspondence to: D. Y. Le Roux, Département de Mathématiques et de Statistique, Université Laval, Québec, QC, Canada G1K 7P4.
†E-mail: dleroux@mat.ulaval.ca

of the non-hydrostatic pressure term may be significant compared with the hydrostatic one, and hence, it cannot be neglected in numerical simulations.

More recently, several authors have developed hydrodynamic models that include the non-hydrostatic pressure term in the simulation of free-surface flows. For example, Casulli and Stelling [4] introduced a semi-implicit fractional step method using a finite difference scheme for the spatial discretization and Casulli [5] added a correction for the free surface to reduce the splitting error. By following the same solution procedure, Mahadevan *et al.* [6] developed a non-hydrostatic mesoscale ocean model by using the finite volume method. Further, Chen [7] introduced a double predictor–corrector semi-implicit finite difference procedure. Stelling and Zijlema [8] presented an accurate approximation of vertical gradient of the non-hydrostatic pressure based on the Preissmann scheme. By adding the non-hydrostatic component, Jankowski [9] updated an existing finite-element (FE) model (in the TELEMAC system) and used equal-order linear interpolation functions for pressure and velocity, i.e. the P_1–P_1 FE pair. All these non-hydrostatic models employ a fractional step (operator-splitting) technique that splits the pressure into its hydrostatic and non-hydrostatic components and divides the differential operator in the momentum equations into several parts according to their physical processes. The original momentum equations are thus split into few simpler equations which are solved more easily.

Instead of using the fractional step technique and the pressure splitting, Huerta and Liu [10] applied the arbitrary Lagrangian–Eulerian (ALE) and the mixed SUPG FE methods for computation of flows with large surface movements. In order to solve the resulting coupled equation system, they used a predictor–multi-corrector scheme. Ramaswamy [11] developed a model based on the ALE technique able to deal with various wave problems and density currents with a free surface as well. He used a velocity correction method based on the Poisson pressure equation and found the surface from the kinematic boundary condition.

In the present work, we develop a fully non-hydrostatic model for two-dimensional vertical free-surface flows by using a non-conforming FE approximation for velocity and salinity (P_1^{NC}) and a linear conforming approximation for free-surface elevation and hydrodynamic pressure (P_1). The employed FE pair is denoted as P_1^{NC}–P_1 [12–14] and has been successfully used in [15] for advection-dominated flows. Further, an accurate representation of the non-linear Rossby modes has been obtained in [16] using this pair. The proposed numerical scheme is validated using three test cases: deepwater standing wave, propagation of a solitary wave in a long channel and the density-driven flows.

This paper is organized as follows. A review of projection methods for Navier–Stokes equations is mentioned in Section 2. The governing equations and the non-hydrostatic fractional step algorithm are presented in Sections 3 and 4, respectively. The FE mixed formulation follows in Section 5. Simulation of three test cases is performed in Section 6 using the proposed FE scheme and some concluding remarks complete the study.

2. REVIEW OF PROJECTION METHODS FOR THE NAVIER–STOKES EQUATIONS

Projection methods have been introduced in [17, 18]. They are time-marching procedures based on a fractional step technique that may be viewed as a predictor–corrector strategy aiming at decoupling incompressibility and viscous diffusion effects. The main idea of these methods is to solve sequentially a number of smaller linear equation systems instead of an iterative solution of a larger one, usually non-linear and slowly converging. The distinction between the direct coupled

DOI: 10.1002/fld

and the fractional decoupled approaches lies in the treatment of the incompressibility constraint. While in the direct method the continuity equation appears explicitly as a constraint on the velocity field, in the decoupled pressure method the momentum and continuity equations are only coupled sequentially and the coupling appears in the corrections that follow from the solution of a derived Poisson equation for pressure.

The space-discretized Navier–Stokes equations are expressed in the matrix form as

$$M\frac{\partial \mathbf{u}}{\partial t}+N(\mathbf{u})\mathbf{u}+K\mathbf{u}+Cp=F \tag{1}$$

$$C^{\mathrm{T}}\mathbf{u}=G \tag{2}$$

where $\mathbf{u}$ and p denote the velocity and the pressure, respectively, M, $N(\mathbf{u})$, K and C are the mass, advection, viscous and gradient matrices, respectively, and F and G are vectors that include boundary conditions on velocity.

In the following, we briefly describe the projection algorithm corresponding to the projection 2 method in [19, 20]. Starting with $n=0$, given u^0 and p^0:

1. Solve the provisional velocity $\tilde{\mathbf{u}}^{n+1}=(\tilde{u}^{n+1},\tilde{w}^{n+1})$

$$\frac{1}{\Delta t}M(\tilde{\mathbf{u}}^{n+1}-\mathbf{u}^n)+N(\mathbf{u}^n)\mathbf{u}^n+K\tilde{\mathbf{u}}^{n+1}+MM_{\mathrm{L}}^{-1}Cp^n=F^n \tag{3}$$

or

$$(M+\Delta t K)\tilde{\mathbf{u}}^{n+1}=M\mathbf{u}^n+\Delta t[F^n-N(\mathbf{u}^n)\mathbf{u}^n-MM_{\mathrm{L}}^{-1}Cp^n] \tag{4}$$

Note that the matrix MM_{L}^{-1} in (3), where M_{L} is the lumped mass matrix, is introduced in [19, 20] in place of the identity matrix (I) in order to improve the stability of the numerical computations. Two techniques are usually employed to perform the lumping. The first one amounts to add to the diagonal elements of the consistent mass matrix the off-diagonal elements so that the total 'mass' associated with a node is conserved [21]. Secondly, mass lumping may be achieved by introducing reduced or inexact quadrature, where the sampling points are the nodes of the element [22]. It is important to emphasize that approximating velocity using the P_1^{NC} FE (see Section 5) leads to a 'naturally' diagonal mass matrix M in (3). This is due to the orthogonality property of the non-conforming linear basis functions [23]. Consequently, we have $M=M_{\mathrm{L}}$ and hence $MM_{\mathrm{L}}^{-1}=I$ in (4) when the P_1^{NC} FE approximation is employed.

2. Find $\mathbf{u}^{n+1}$ by solving

$$\frac{1}{\Delta t}M(\mathbf{u}^{n+1}-\tilde{\mathbf{u}}^{n+1})+MM_{\mathrm{L}}^{-1}C(p^{n+1}-p^n)=0 \tag{5}$$

or

$$\mathbf{u}^{n+1}=\tilde{\mathbf{u}}^{n+1}-\Delta t M_{\mathrm{L}}^{-1}C\phi^{n+1} \tag{6}$$

where $\phi^{n+1}=p^{n+1}-p^n$ is the solution to the following Poisson equation:

$$C^{\mathrm{T}}M_{\mathrm{L}}^{-1}C\phi^{n+1}=\frac{1}{\Delta t}(C^{\mathrm{T}}\tilde{\mathbf{u}}^{n+1}-G) \tag{7}$$

obtained by combining (6) and the incompressibility constraint (2) at time $n+1$.

DOI: 10.1002/fld

3. Finally, update the pressure

$$p^{n+1} = p^n + \phi^{n+1} \tag{8}$$

We now describe the governing equations that are employed in the proposed scheme.

3. GOVERNING EQUATIONS

We consider a physical domain that is bounded vertically by the free surface $z = \eta(x,t)$ and the bottom $z = H(x)$, i.e. the distance between the bottom and the reference level $z = 0$, as shown in Figure 1. The computational domain variability is taken into account by standard σ-mesh structure which is well suited to many geophysical applications. The σ-transformation involves linear stretching of the mesh between the bed and the free surface. This has the advantage of avoiding the remeshing procedure that is usually necessary when Cartesian coordinates are used, due to the moving free surface. The transformation from the physical (x,z,t) to the σ-transformed (x,σ,t) coordinates is based on the following mapping:

$$\sigma = \frac{z-H}{\eta-H}$$

and for a variable $Q(x,z,t)$ we have

$$\frac{\mathrm{d}Q}{\mathrm{d}t}(x,z,t) = \frac{\partial Q}{\partial t}(x,\sigma) + u\frac{\partial Q}{\partial x}(x,\sigma,t) + w_\sigma \frac{\partial Q}{\partial \sigma}(x,t)$$

where w_σ is the following transformed vertical velocity component w in σ-coordinates (x,σ):

$$w_\sigma = \frac{\mathrm{d}\sigma}{\mathrm{d}t} = \frac{\partial \sigma}{\partial t}(x,z) + u\frac{\partial \sigma}{\partial x}(x,z,t) + w\frac{\partial \sigma}{\partial z}(x,t)$$

For the sake of simplicity the σ-mesh structure, although used in the model and numerical simulations, is not formally written in the remaining of the paper.

The governing two-dimensional, primitive variable equations describing free-surface flows are the Navier–Stokes equations. The momentum equations are

$$\frac{\partial u}{\partial t} + u\frac{\partial u}{\partial x} + w\frac{\partial u}{\partial z} = -\frac{1}{\rho}\frac{\partial p}{\partial x} + \mu_x \frac{\partial^2 u}{\partial x^2} + \mu_z \frac{\partial^2 u}{\partial z^2} \tag{9}$$

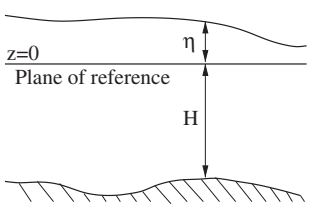

Figure 1. A layer of fluid with varying bottom and free surface.

DOI: 10.1002/fld

$$\frac{\partial w}{\partial t}+u\frac{\partial w}{\partial x}+w\frac{\partial w}{\partial z}=-\frac{1}{\rho}\frac{\partial p}{\partial z}-g+\mu_x\frac{\partial^2 w}{\partial x^2}+\mu_z\frac{\partial^2 w}{\partial z^2} \tag{10}$$

where $\mathbf{u}=(u(x,z,t),w(x,z,t))$ is the velocity field with u and w being the velocity components in the x- and z-directions, respectively, $\rho(x,z)$ is the density field, g is the gravitational acceleration, and μ_x and μ_z are the eddy viscosity coefficients in the x- and z-directions, respectively.

The mass conservation is expressed by the incompressibility condition

$$\nabla\cdot\mathbf{u}=\frac{\partial u}{\partial x}+\frac{\partial w}{\partial z}=0 \tag{11}$$

The kinematic condition at the free surface is

$$\frac{\partial \eta}{\partial t}+u_\eta\frac{\partial \eta}{\partial x}-w_\eta=0 \tag{12}$$

where $\eta(x,t)$ is the free-surface elevation and u_η and w_η are, respectively, the restrictions of the velocity components u and w at the free surface.

The transport equation for salinity $S(x,z)$ is expressed as

$$\frac{\partial S}{\partial t}+\mathbf{u}\cdot\nabla S=v_x\frac{\partial^2 S}{\partial x^2}+v_z\frac{\partial^2 S}{\partial z^2} \tag{13}$$

where v_x and v_z are the eddy dispersion coefficients in the x- and z-directions, respectively. The values of ρ are obtained from S by using the international equation of state for seawater (IES80) [24] with constant temperature and pressure.

The pressure p in (9) and (10) can be decomposed into the sum of its hydrostatic and non-hydrostatic components denoted by p_{H} and π, respectively, with

$$p=p_{\mathrm{H}}+\pi=\rho g(\eta-z)+\pi \tag{14}$$

The momentum equations (9) and (10) can thus be expressed as

$$\frac{\mathrm{d}u}{\mathrm{d}t}=\frac{\partial u}{\partial t}+u\frac{\partial u}{\partial x}+w\frac{\partial u}{\partial z}=-g\frac{\partial \eta}{\partial x}-\frac{1}{\rho}\frac{\partial \pi}{\partial x}+\mu_x\frac{\partial^2 u}{\partial x^2}+\mu_z\frac{\partial^2 u}{\partial z^2} \tag{15}$$

$$\frac{\mathrm{d}w}{\mathrm{d}t}=\frac{\partial w}{\partial t}+u\frac{\partial w}{\partial x}+w\frac{\partial w}{\partial z}=-\frac{1}{\rho}\frac{\partial \pi}{\partial z}+\mu_x\frac{\partial^2 w}{\partial x^2}+\mu_z\frac{\partial^2 w}{\partial z^2} \tag{16}$$

We now include the pressure splitting (14) in the fractional step algorithm.

4. NON-HYDROSTATIC FRACTIONAL STEP ALGORITHM

The velocity time derivative is split into

$$\frac{\partial \mathbf{u}}{\partial t}\simeq\frac{\mathbf{u}^{n+1}-\tilde{\mathbf{u}}^{n+1}}{\Delta t}+\frac{\tilde{\mathbf{u}}^{n+1}-\mathbf{u}^{n}}{\Delta t} \tag{17}$$

DOI: 10.1002/fld

where $\tilde{\mathbf{u}}^{n+1}$ is a provisional velocity field, which does not need to satisfy the incompressibility condition (2). Given the initial conditions η^0, π^0 and $\mathbf{u}^0$ and employing (17), Equations (15)–(16) are split into two sets of equations

$$\frac{\tilde{u}^{n+1}-u^n}{\Delta t}+u^n\frac{\partial u^n}{\partial x}+w^n\frac{\partial u^n}{\partial z}=-g\frac{\partial \eta^n}{\partial x}-\frac{1}{\rho}\frac{\partial \pi^n}{\partial x}+\mu_x\frac{\partial^2 u^{n+1}}{\partial x^2}+\mu_z\frac{\partial^2 u^{n+1}}{\partial z^2} \tag{18}$$

$$\frac{u^{n+1}-\tilde{u}^{n+1}}{\Delta t}=-\frac{1}{\rho}\frac{\partial \pi^{n+1}}{\partial x}+\frac{1}{\rho}\frac{\partial \pi^n}{\partial x} \tag{19}$$

$$\frac{\tilde{w}^{n+1}-w^n}{\Delta t}+u^n\frac{\partial w^n}{\partial x}+w^n\frac{\partial w^n}{\partial z}=-\frac{1}{\rho}\frac{\partial \pi^n}{\partial z}+\mu_x\frac{\partial^2 w^{n+1}}{\partial x^2}+\mu_z\frac{\partial^2 w^{n+1}}{\partial z^2} \tag{20}$$

$$\frac{w^{n+1}-\tilde{w}^{n+1}}{\Delta t}=-\frac{1}{\rho}\frac{\partial \pi^{n+1}}{\partial z}+\frac{1}{\rho}\frac{\partial \pi^n}{\partial z} \tag{21}$$

and we let $\phi^{n+1}=\pi^{n+1}-\pi^n$ in (19) and (21). Zero normal velocity and free slip conditions are imposed at solid boundaries and, at the free surface, the zero Neumann boundary condition is set for the two velocity components.

First, $\tilde{u}^{n+1}$ and $\tilde{w}^{n+1}$ are obtained from (18) and (20). Note that the viscous terms may be computed at time n instead of $n+1$, without affecting noticeably the length of the time step in the numerical tests performed in Section 6. This is also expected in many geophysical applications, where the amount of viscosity is usually small. As previously mentioned, approximating $\mathbf{u}$ and $\tilde{\mathbf{u}}$ in (18) and (20) using the P_1^{NC} FE leads to diagonal velocity mass matrices, and hence to a tremendous saving in the computational cost and memory requirement. Indeed, $\tilde{u}^{n+1}$ and $\tilde{w}^{n+1}$ are computed without the need for solving linear systems.

In a second step, by combining (19) and (21) and imposing the incompressibility condition $\nabla\cdot\mathbf{u}^{n+1}=0$, we obtain the following equation for the hydrodynamic pressure:

$$\nabla^2\phi^{n+1}=\frac{\rho}{\Delta t}\nabla\cdot\tilde{\mathbf{u}}^{n+1}+\frac{1}{\rho}\left(\frac{\partial \phi^{n+1}}{\partial x}\frac{\partial \rho}{\partial x}+\frac{\partial \phi^{n+1}}{\partial z}\frac{\partial \rho}{\partial z}\right) \tag{22}$$

with the boundary conditions

$$\phi^{n+1}=0 \quad \text{on the free surface} \tag{23}$$

$$\frac{\partial \phi^{n+1}}{\partial \mathbf{n}}=0 \quad \text{on the solid boundaries} \tag{24}$$

For the hydrodynamic pressure, the zero Dirichlet condition is set at the free surface (by referring to Figure 1, $\pi=0$ at $z=\eta$) and the zero Neumann condition ($\partial\pi/\partial\mathbf{n}=0$) is imposed at all solid boundaries (lateral and bottom boundaries). Note that $\mathbf{n}$ is the outer unit normal to the domain boundary.

Once ϕ^{n+1} is calculated, the final velocity field $\mathbf{u}^{n+1}$ is then obtained from (19) to (21)

$$\mathbf{u}^{n+1}=\tilde{\mathbf{u}}^{n+1}-\frac{\Delta t}{\rho}\nabla\phi^{n+1} \tag{25}$$

DOI: 10.1002/fld

and the free-surface elevation η^{n+1} is computed from (12) by using a θ-scheme

$$\frac{\eta^{n+1}-\eta^n}{\Delta t}+\theta u_\eta^{n+1}\frac{\partial \eta^{n+1}}{\partial x}+(1-\theta)u_\eta^n\frac{\partial \eta^n}{\partial x}-w_\eta^{n+1}=0 \tag{26}$$

where θ is a real parameter ranging from 0 to 1.

Finally, the hydrodynamic pressure is updated

$$\pi^{n+1}=\pi^n+\phi^{n+1} \tag{27}$$

We now introduce the spatial discretization scheme using the P_1^{NC}–P_1 FE pair.

5. THE P_1^{NC}–P_1 DISCRETIZATION SCHEME

Let $\mathscr{T}_h$ be a partition of the domain Ω into N_K triangles and K_i and Γ be the set of N_Γ interior edges $\Gamma_l=\partial K_i\cap\partial K_j$ with $i>j$, where ∂K_i denotes the boundary of triangle K_i. For each edge Γ_l, we associate a unique unit normal $\mathbf{n}$ that points from K_i to K_j.

The variational or weak formulation of (18) and (20) is built in such a way that the solution for velocity can be discontinuous between the elements K_i. We let $V=\{v\in L^2(\Omega): v|_{K_i}\in H^1(K_i),\ \forall K_i\in\mathscr{T}_h\}$, where the Sobolev space $H^1(\Omega)$ is the space of functions in the square-integrable space $L^2(\Omega)$, whose first derivatives belong to $L^2(\Omega)$. We multiply (18) and (20) by a test function φ belonging to V and integrate over the domain Ω. By following the same procedure as in [15, 16], where the advection terms are integrated by parts, we obtain

$$\begin{aligned}&\sum_{i=1}^{N_K}\int_{K_i}\left(\frac{\tilde{u}^{n+1}-u^n}{\Delta t}\varphi-u^n\nabla\cdot(\mathbf{u}^n\varphi)\right)\mathrm{d}\Omega+\sum_{l=1}^{N_\Gamma}\int_{\Gamma_l}\langle u^n\mathbf{u}^n\cdot\mathbf{n}\rangle_\lambda[\varphi]\,\mathrm{d}\Gamma\\&\quad=\sum_{i=1}^{N_K}\int_{K_i}\left(-g\frac{\partial\eta^n}{\partial x}\varphi-\frac{1}{\rho}\frac{\partial\pi^n}{\partial x}\varphi-\mu_x\frac{\partial u^{n+1}}{\partial x}\frac{\partial\varphi}{\partial x}-\mu_z\frac{\partial u^{n+1}}{\partial z}\frac{\partial\varphi}{\partial z}\right)\mathrm{d}\Omega\quad\forall\varphi\in V\end{aligned} \tag{28}$$

$$\begin{aligned}&\sum_{i=1}^{N_K}\int_{K_i}\left(\frac{\tilde{w}^{n+1}-w^n}{\Delta t}\varphi-w^n\nabla\cdot(\mathbf{u}^n\varphi)\right)\mathrm{d}\Omega+\sum_{l=1}^{N_\Gamma}\int_{\Gamma_l}\langle w^n\mathbf{u}^n\cdot\mathbf{n}\rangle_\lambda[\varphi]\,\mathrm{d}\Gamma\\&\quad=\sum_{i=1}^{N_K}\int_{K_i}\left(-\frac{1}{\rho}\frac{\partial\pi^n}{\partial z}\varphi-\mu_x\frac{\partial w^{n+1}}{\partial x}\frac{\partial\varphi}{\partial x}-\mu_z\frac{\partial w^{n+1}}{\partial z}\frac{\partial\varphi}{\partial z}\right)\mathrm{d}\Omega\quad\forall\varphi\in V\end{aligned} \tag{29}$$

where $\mathrm{d}\Omega=\mathrm{d}x\,\mathrm{d}z$ is the area element and $\langle\zeta\rangle_\lambda=(\frac{1}{2}+\lambda)\zeta|_{K_i}+(\frac{1}{2}-\lambda)\zeta|_{K_j}$ and $[\zeta]=\zeta|_{K_i}-\zeta|_{K_j}$, respectively, denote the average and the jump of ζ on the edge Γ_l, where $|\Gamma_l|$ is the length of Γ_l. The parameter $\lambda\in[-\frac{1}{2},\frac{1}{2}]$ permits to orient the advective flux. Choosing $\lambda=0$ leads to a centred advection scheme which usually generates false extrema for strong advective flows since it is directionally symmetric, contrary to advection. A more stable scheme, interpreted as an upwind scheme, can be derived by selecting $\lambda=\frac{1}{2}\mathrm{sign}(\mathbf{u}.\mathbf{n})$, as in [15], i.e. by taking into account the directionally oriented nature of the flow.

DOI: 10.1002/fld

The weak formulation of (13) is also built in such a way that the solution for salinity can be discontinuous between the elements K_i. By following the same procedure as in [15] and previously in (28) and (29), we obtain

$$\sum_{i=1}^{N_K}\int_{K_i}\left(\frac{S^{n+1}-S^n}{\Delta t}\varphi - S^n\nabla\cdot(\mathbf{u}^n\varphi)\right)\mathrm{d}\Omega+\sum_{l=1}^{N_\Gamma}\int_{\Gamma_l}\langle S^n\mathbf{u}^n\cdot\mathbf{n}\rangle_\lambda[\varphi]\,\mathrm{d}\Gamma$$
$$=\sum_{i=1}^{N_K}\int_{K_i}\left(-v_x\frac{\partial S^{n+1}}{\partial x}\frac{\partial\varphi}{\partial x}-v_z\frac{\partial S^{n+1}}{\partial z}\frac{\partial\varphi}{\partial z}\right)\mathrm{d}\Omega\quad\forall\varphi\in V \tag{30}$$

where natural boundary conditions are used to perform the integration by parts of the dispersion terms.

Let ϕ and η be in a subspace W of $H^1(\Omega)$. The weak formulation of (22) and (26) requires the test functions χ and ψ belong to W, such that

$$-\int_\Omega\nabla\phi^{n+1}\cdot\nabla\chi\,\mathrm{d}\Omega+\int_{\partial\Omega}\nabla\phi^{n+1}\cdot\mathbf{n}\,\chi\,\mathrm{d}\sigma=-\frac{\rho}{\Delta t}\int_\Omega\tilde{\mathbf{u}}^{n+1}\cdot\nabla\chi\,\mathrm{d}\Omega+\frac{\rho}{\Delta t}\int_{\partial\Omega}\tilde{\mathbf{u}}^{n+1}\cdot\mathbf{n}\,\chi\,\mathrm{d}\sigma$$
$$+\int_\Omega\frac{1}{\rho}\left(\frac{\partial\phi^{n+1}}{\partial x}\frac{\partial\rho}{\partial x}+\frac{\partial\phi^{n+1}}{\partial z}\frac{\partial\rho}{\partial z}\right)\chi\,\mathrm{d}\Omega \tag{31}$$

$$\int_\Omega\left(\frac{\eta^{n+1}-\eta^n}{\Delta t}\right)\psi\,\mathrm{d}\Omega+\int_\Omega\theta u^{n+1}\frac{\partial\eta^{n+1}}{\partial x}\psi\,\mathrm{d}\Omega=-\int_\Omega(1-\theta)u_\eta^n\frac{\partial\eta^n}{\partial x}\psi\,\mathrm{d}\Omega+\int_\Omega w_\eta^{n+1}\psi\,\mathrm{d}\Omega \tag{32}$$

where $\mathrm{d}\sigma$ denotes counter-clockwise integration around the boundary $\partial\Omega$. Contrary to $\chi(x,z)$, the test function ψ depends only on x. By applying the boundary conditions (23) and (24), the boundary integral in the LHS of (31) vanishes. Note that the weak formulation of (25) is

$$\int_\Omega\mathbf{u}^{n+1}\cdot\boldsymbol{\varphi}\,\mathrm{d}\Omega=\int_\Omega\tilde{\mathbf{u}}^{n+1}\cdot\boldsymbol{\varphi}\,\mathrm{d}\Omega-\int_\Omega\frac{\Delta t}{\rho}\nabla\phi^{n+1}\cdot\boldsymbol{\varphi}\,\mathrm{d}\Omega \tag{33}$$

where the x- or the z-component of $\boldsymbol{\varphi}$ is formally denoted by φ, and for (27) we obtain

$$\int_\Omega\pi^{n+1}\chi\,\mathrm{d}\Omega=\int_\Omega(\pi^n+\phi^{n+1})\chi\,\mathrm{d}\Omega \tag{34}$$

Here, we choose to approximate S in the same space than the velocity variables (using the P_1^{NC} FE approximation) and not with continuous P_1 FE as for ϕ. This choice is motivated by the fact that in [15, 16] very good results have been obtained for the advection equation using the P_1^{NC} FE compared with the continuous P_1 one. Consequently, we admit a small inconsistency which seems to have no effect in the numerical tests performed in this paper.

The Galerkin FE method employing the P_1^{NC}–P_1 pair is now used to spatially discretize (28)–(34). The P_1^{NC} discretization approximates the velocity components u and w and the salinity S

DOI: 10.1002/fld

at triangle midside nodes, and the linear basis function satisfies

$$\phi_M(x_M, z_M) = 1 \tag{35}$$

$$\phi_M(x_N, z_N) = 0 \quad \text{if } M \neq N \tag{36}$$

at midside nodes M and N of coordinates (x_M, z_M) and (x_N, z_N), respectively. The P_1^{NC} basis function is hence zero outside the element's two-triangle support. Since this particular representation of velocity is continuous only across triangle boundaries at midedge points, and discontinuous everywhere else around a triangle boundary, this element is termed non-conforming (NC) in the FE literature. Standard piecewise linear continuous basis functions (P_1) are used to approximate the surface elevation at triangle vertices.

The Galerkin method approximates the solution of (28)–(34) in finite-dimensional subspaces. For triangle $K \in \mathscr{T}_h$, let $P_1(K)$ denote the space of linear polynomials on K. The discrete solution $\mathbf{u}_h = (u_h, w_h)$ and S_h sought belong to a finite-dimensional space $\mathbf{V}_h$ defined to be the set of functions whose restriction on K belongs to $P_1(K) \times P_1(K)$, with $\mathbf{u}_h$ and S_h being continuous only at the midpoints of each face of $\mathscr{T}_h$, and $\mathbf{u}_h$ satisfying the velocity boundary conditions. Since velocity nodes are located at triangle midedge points, the direction of the local tangential vector $\mathbf{t}_p$ is uniquely defined along the boundary. The discrete solutions ϕ_h and π_h are sought in a finite-dimensional subspace W_h, where W_h is defined to be the set of functions whose restriction on K belongs to $P_1(K)$, and being continuous at each vertex of $\mathscr{T}_h$.

Introducing the FE basis leads to a Fe statement as in (28)–(34) but with u, w, ϕ and π replaced by the FE trial functions u_h, w_h, ϕ_h and π_h. We then decompose the integrals over the domain Ω into triangle contributions and u_h, w_h, ϕ_h and π_h are expanded over all triangles of $\mathscr{T}_h$.

The most useful property of the P_1^{NC} basis functions is their orthogonality property [23]

$$\int_\Omega \varphi_M \varphi_N \, \mathrm{d}\Omega = \frac{A_M}{3} \delta_{MN} \tag{37}$$

where A_M is the area of the support of φ_M, and δ_{MN} is the Kronecker delta. Such an unusual property increases the computational efficiency of the model. Indeed, in (33), and also in (28)–(30), if the viscous and dispersion terms are evaluated at time n (which is the case in the present study and for many geophysical applications), the mass matrices are diagonal. This leads to a tremendous saving in the computational cost and memory requirement and only linear systems for ϕ and η in (31) and (32), not for velocity and salinity, need to be solved. Such a saving is enhanced by considering that ϕ is located at vertex nodes (there are usually three times less vertices than midside nodes) and η and χ depends only on x.

Finally, it seems that we have committed a variational crime [23] by omitting the boundary viscous terms in (28) and (29). As shown in [15], those terms naturally vanish by using the P_1^{NC} discretization.

6. NUMERICAL EXPERIMENTS

The present non-hydrostatic numerical model is validated using three test cases including deepwater standing wave, propagation of a solitary wave in a long channel and the density-driven flow. In this section, we choose $\theta = 1$ in (32); however, the use of $\theta = \frac{1}{2}$ leads to similar results with insignificant

DOI: 10.1002/fld

differences. Further, all the experiments are conducted with a flat bottom, i.e. H is assumed to be constant.

6.1. Standing wave in a closed basin

We consider here a small amplitude deepwater standing wave in a closed basin. As the initial condition, a sloped free surface and no motion is taken, i.e. a configuration with maximum potential energy. A wave motion begins and in the moment, when the free surface is horizontal, the whole available potential energy has been exchanged into kinetic one. When the highest water level at the opposite wall is reached, the maximum potential and minimum kinetic energy state is achieved again, just as at the very beginning of the simulation.

The basin is shown in Figure 2, with $H=10\,\mathrm{m}$ and $L=10\,\mathrm{m}$. The initial free surface is

$$\eta(x,0)=\eta_0\cos(kx), \quad 0<x<L$$

and a zero initial velocity is assumed. We let the initial wave amplitude wave to be $\eta_0=0.1\,\mathrm{m}$ and $k=\pi/L$. According to the small amplitude wave theory [25, 26], with $\eta_0 \ll H$, describing the resulting wave motion in the plane (x,z), the solution for free-surface elevation η, velocity components (u,w) and non-hydrostatic pressure π are

$$\eta(x,t)=\eta_0\cos(kx)\cos(\omega t)$$

$$u(x,z,t)=-\omega\eta_0\frac{\sinh[k(z+H)]}{\cosh(kH)}\sin(kx)\sin(\omega t)$$

$$w(x,z,t)=\omega\eta_0\frac{\cosh[k(z+H)]}{\sinh(kH)}\cos(kx)\sin(\omega t)$$

$$\pi(x,z,t)=-\rho g\eta+\rho g\eta_0\frac{\cosh[k(z+H)]}{\cosh(kH)}\cos(kx)\cos(\omega t)$$

The proper initial conditions for $t=0$ are

$$\eta(x,0)=\eta_0\cos(kx), \quad u(x,0)=0, \quad w(x,0)=0$$

$$\pi(x,0)=\rho g\eta_0\frac{\cosh[k(z+H)]}{\cosh(kH)}\cos(kx)$$

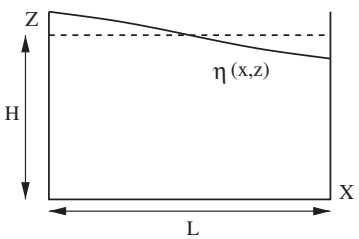

Figure 2. A standing wave in a closed basin.

DOI: 10.1002/fld

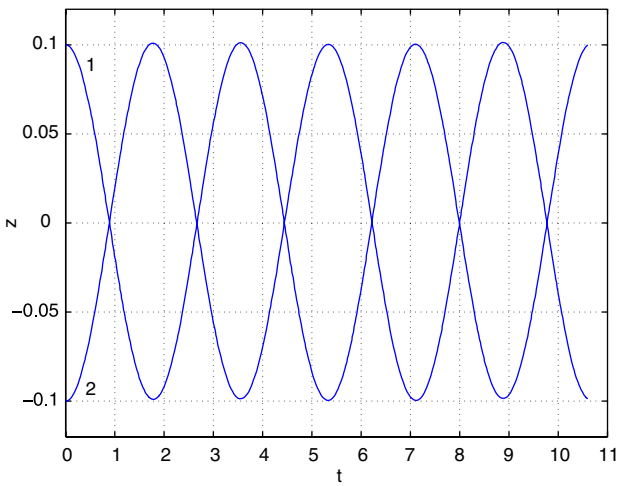

Figure 3. Time series for the simulated free surface elevation at the boundary edges $x=0$ m, where $\eta(0,t)$ is represented by curve 1, and $x=L=10$ m, where $\eta(L,t)$ is represented by curve 2, after 11 s of simulation.

We take $g=10\,\mathrm{m/s^2}$ and $\rho=1000\,\mathrm{kg/m^3}$. Applying the general small amplitude wave theory, the wave celerity is $c=[(g/k)\tanh(kH)]^{1/2}=5.63\,\mathrm{m/s}$ and the period of oscillation is $T=3.55$ s. The mesh resolution is 0.2 m in both horizontal and vertical directions, with 2601 nodes and 5000 triangular elements. The model is run for 11 s using a time step of 0.01 s. In Figure 3, time series for the simulated surface elevation are displayed at the boundary edges $x=0$ m (curve 1) and $x=10$ m (curve 2) at the end of the simulation, i.e. after 11 s. The amplitude remains constant and approximately equal to the initial one (0.1 m). The wave period for the simulated oscillation is about 3.55 s, which corresponds to that calculated from short wave theory. It is illustrative to show the results when both the states of maximum and minimum kinetic energy are achieved. Theoretically, the maximum kinetic energy corresponds to one-fourth of the oscillation period, i.e. approximately 0.89 s, and the minimum kinetic energy corresponds to one full period.

In Figure 4, the velocity and hydrodynamic pressure are shown for one-fourth oscillation period ($t=0.89$ s). From the analytical solution described above, the horizontal velocity should range between 0 and 0.17634 m/s and the vertical one at the free surface should range from -0.1777 to 0.1777 m/s. The numerical results range from 0 to 0.1775 m/s for the horizontal velocity and from -0.1753 to 0.1782 m/s for the vertical one. They are thus quite close to the analytical ones. For the hydrodynamic pressure, it is obvious that, at $t=T/4=\pi/2\omega$, it should vanish. The maximum value obtained here (28.74 Pa) is very small. The observed small oscillations are due to the fact that the hydrodynamic pressure has a very weak amplitude (28.74 Pa) compared with the hydrostatic one (100 000 Pa), leading to a ratio of 0.03%.

In Figure 5, the results are shown for one full period (3.55 s) when the state of minimum kinetic energy is achieved again. The analytical solution gives $u=w=0$ everywhere and the hydrodynamic pressure should range from -1000 to 1000 Pa. The computed results, less than 5×10^{-3} m/s for the velocities and from -941.72 to 885.86 Pa for the hydrodynamic pressure, are again close to the analytical ones. The fact that the fluid is not completely still after one period may suggest that the momentum is totally null. In the numerical model, the non-linear terms (convective) are not

DOI: 10.1002/fld

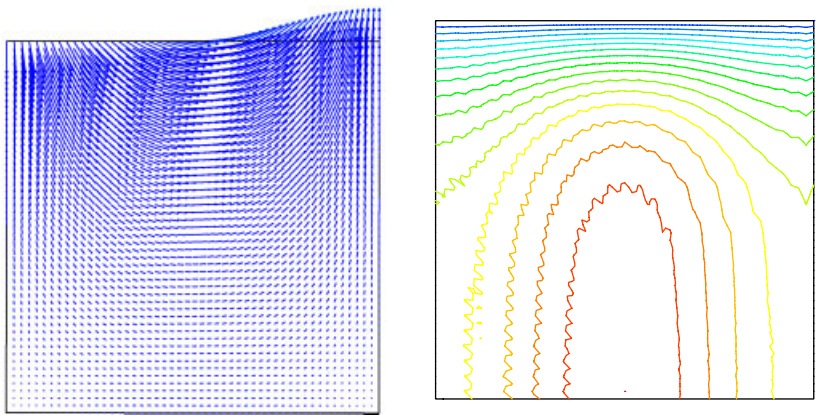

Figure 4. Velocity (left) and hydrodynamic pressure (right) for one-fourth of the oscillation period. The horizontal velocity component u ranges between 0 and 0.1775 m/s, and the vertical velocity component w ranges between -0.1753 and 0.1782 m/s. For the hydrodynamic pressure 15 isolines range between 0 and 28.74 Pa. The maximum value for the free-surface elevation is 4.56×10^{-4} m.

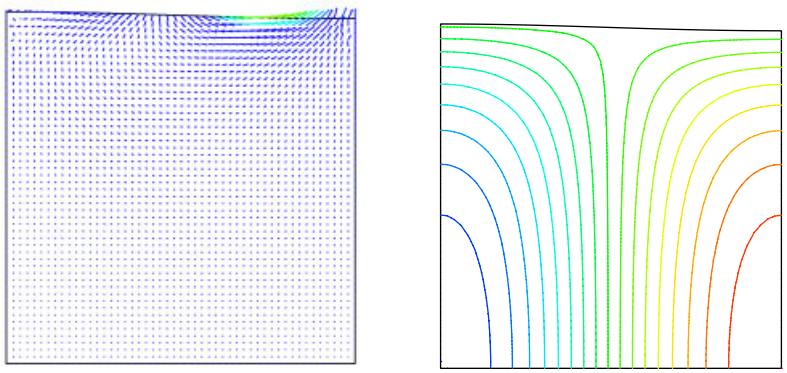

Figure 5. Velocity and hydrodynamic pressure for one oscillation period. The horizontal velocity component u ranges between -1.34×10^{-3} and 4.86×10^{-3} m/s. The vertical velocity component w ranges between -8.74×10^{-4} and 1.53×10^{-3} m/s. For the hydrodynamic pressure 17 isolines range between -941.72 and 885.86 Pa. The maximum value of the free-surface elevation is 0.10121 m.

set to zero and they could contribute to perturbate the phase between the surface elevation and the velocity.

6.2. *Solitary wave propagation in a long channel*

The analysis of solitary wave propagation is important for the design of breakwaters or sea walls and other offshore structures. The solitary wave is defined as a single elevation above the surrounding undisturbed water level, producing a definite transport in the direction of wave propagation only. The wave travels without change of shape and with essentially constant celerity.

DOI: 10.1002/fld

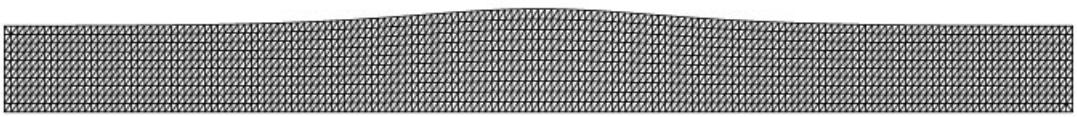

Figure 6. The initial wave shape and the mesh used in test of Section 6.2.

Laitone's approximation [27] of a solitary wave is frequently used for comparative study. In these approximations, velocity, pressure and free-surface elevation can be expressed as

$$\eta(x,t)=H+\xi\,\mathrm{sech}^2\left(\sqrt{\frac{3}{4}\frac{\xi}{H^3}}(x-ct)\right) \tag{38}$$

$$u(x,z,t)=\sqrt{gH}\,\frac{\xi}{H}\,\mathrm{sech}^2\left(\sqrt{\frac{3}{4}\frac{\xi}{H^3}}(x-ct)\right) \tag{39}$$

$$w(x,z,t)=\sqrt{3gH}\left(\frac{\xi}{H}\right)^{3/2}\left(\frac{z}{H}\right)\mathrm{sech}^2\left(\sqrt{\frac{3}{4}\frac{\xi}{H^3}}(x-ct)\right)\tanh\left(\sqrt{\frac{3}{4}\frac{\xi}{H^3}}(x-ct)\right) \tag{40}$$

$$p(x,z,t)=\rho g(\eta-z) \tag{41}$$

$$c=\sqrt{gH\left(1+\frac{\xi}{H}\right)} \tag{42}$$

where ξ and H are the initial wave height and the still water depth, respectively.

We use a rectangular domain with $H=10\,\mathrm{m}$ and a length $L=160\,\mathrm{m}$. The initial wave crest is located in the middle of the domain with a height of 2 m (see Figure 6). We choose $g=9.8\,\mathrm{m/s^2}$ and $\rho=1000\,\mathrm{kg/m^3}$, and the time step $\Delta t=0.02\,\mathrm{s}$ is used. Computed wave profile, velocity and pressure at elapsed times 7.7 and 15 s are shown in Figures 7 and 8, respectively. The wave speed of a solitary wave given by Laitone's approximation (42) is $c=10.84\,\mathrm{m/s}$. Because the half-horizontal length of the channel is 80 m, the wave crest arrives at the right-hand vertical wall at time 7.7 s. This theoretical value compares well with the computed one, which is 7.68 s.

The run-up height of a solitary wave on a vertical wall R can be obtained by Laitone's approximation:

$$\frac{R}{H}=10+2\frac{\xi}{H}+\frac{1}{2}\left(\frac{\xi}{H}\right)^2$$

With the choice $\xi/H=0.2$, we obtain $R=14.2\,\mathrm{m}$. The numerical value computed by our model is $R=14.29\,\mathrm{m}$, while Ramaswamy [11] obtained $R=14.48\,\mathrm{m}$. At $t=15\,\mathrm{s}$, the wave crest returns at its initial position and its height is 11.98 m. In this test case, the computed pressure is almost hydrostatic which suits well with (41). Here, the use of the non-hydrostatic component π does not perturb the solution of this quasi-hydrostatic flow, and its value is negligible compared with the hydrostatic component of the pressure.

DOI: 10.1002/fld

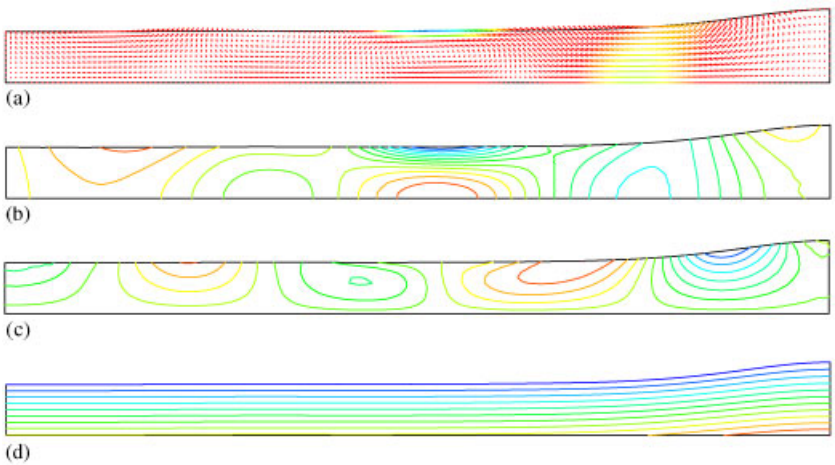

Figure 7. Computed solutions at time $t = 7.7$ s: (a) the velocity field; (b) the velocity component u ranges between -0.277 and 0.116 m/s; (c) the velocity component w ranges between -0.118 and 0.0724 m/s; and (d) the pressure ranges between 0 and 131 920 Pa. All the results are shown with 11 isolines.

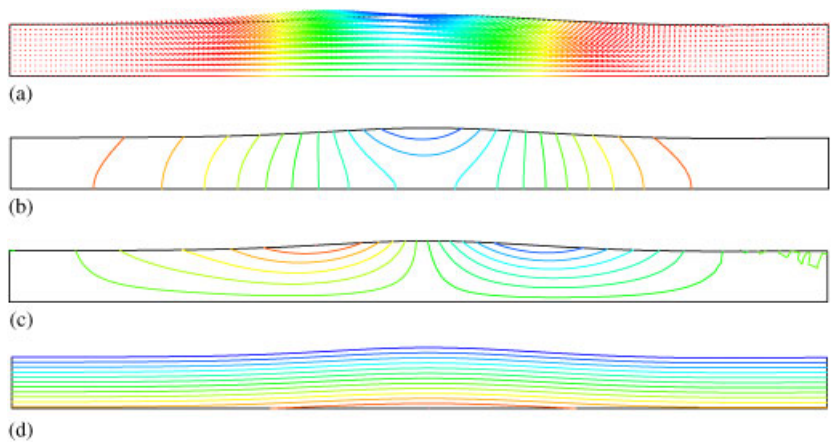

Figure 8. Computed solutions at time $t = 15$ s: (a) the velocity field; (b) the velocity component u ranges between -2.181 and 0.166 m/s; (c) the velocity component w ranges between -0.588 and 0.503 m/s; and (d) the pressure ranges between 0 and 115 143 Pa. All the results are shown with 11 isolines.

As we compare the numerical solution with an approximative one, we cannot quantitatively express the difference between the two. However, the test case has been chosen to fit with the Laiton's approximation and the numerical solution agrees very correctly with it.

6.3. Analysis of density flow

A density flow can be defined as a flow which is mainly driven by pressure gradient that results from the difference in the fluid densities. Examples include a muddy underflow in a lake or

DOI: 10.1002/fld

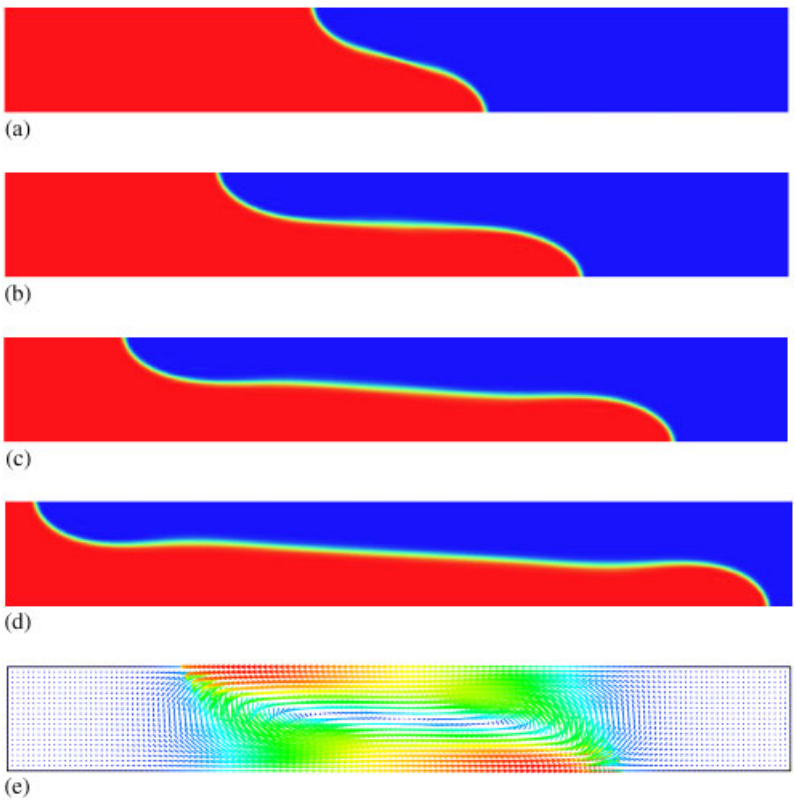

Figure 9. Computed salinity distribution for the low density contrast case at times: (a) 25 s; (b) 50 s; (c) 75 s; and (d) 100 s; and (e) the velocity field at $t=50$ s where the minimum (blue) and maximum (red) values of u and w are $(-0.1028, 0.1043)$ and $(-0.0456, 0.0453)$, respectively.

ocean, a moving atmospheric cold front and the mixing of fluids in many chemical engineering circumstances. We study here two examples of density flows: the first with a small difference in density and the second with a significant difference in density. Note that in both experiments the lack of mesh resolution prevents the Kelvin–Helmholtz instability to develop.

In the first experiment, a rectangular basin with a length $L=30$ m and a depth $H=4$ m has a gate at the half length of the basin that separates fresh water (right with $S=0$ psu) from salty water (left with $S=1$ psu). A 150×20 mesh is used (both horizontal and vertical resolutions are 0.2 m) and the time step is 0.05 s. A low density contrast is considered where the two fluids have the density values 1000.722 and 999.972 kg/m^3 and $g=10\,\mathrm{m/s^2}$. The fluid viscosity is $\mu_x=\mu_z=0.001\,\mathrm{m^2/s}$, and the eddy dispersion coefficients for the salinity in (13) are $\nu_x=0.01\,\mathrm{m^2/s}$ and $\nu_z=0\,\mathrm{m^2/s}$. At initial time the impermeable gate is removed and water starts to move under the baroclinic force caused by the horizontal density gradient. In Figure 9, the salinity distribution is shown at times $t=25, 50, 75$ and 100 s. The velocity field is shown at time $t=50$ s and the maximum velocity calculated by the model in the bottom layer is nearly horizontal at 0.106 m/s.

DOI: 10.1002/fld

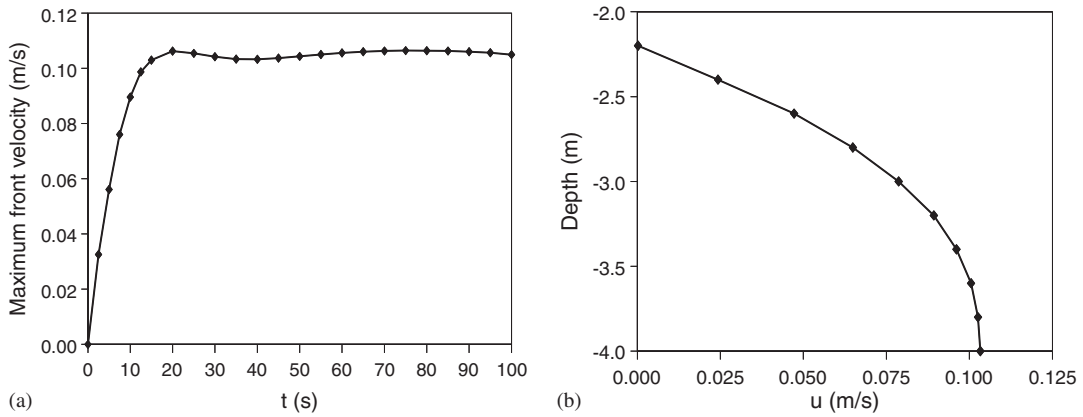

Figure 10. For the bottom layer: (a) maximum front velocity *versus* time and (b) velocity profile at $t=50\,\mathrm{s}$.

Based on the conversion of potential to kinetic energy using the inviscid frictionless Bernoulli equation [28], the following formula

$$u=\frac{\sqrt{2}}{2}\sqrt{\frac{\rho_2-\rho_1}{\rho_2+\rho_1}gH} \tag{43}$$

gives an estimation of the front mean velocity, i.e. 0.0866 m/s, for $\rho_1=1000.722\,\mathrm{kg/m^3}$ and $\rho_2=999.972\,\mathrm{kg/m^3}$. The model maximum front velocity, shown in Figure 10(a), is not the best parameter to be compared with the estimated value obtained from (43). In order to obtain a meaningful comparison, the velocity profile of the moving layer, shown in Figure 10(b), has been numerically integrated from the bottom to a depth where the velocity is almost null, i.e. very near the half depth. The resulting mean front velocity, 0.0728 m/s, is obtained and it is found to be smaller than the predicted value 0.0866 m/s in (43). We argue that this behaviour is physically coherent because the Bernoulli equation does not take into account the non-linear effects due to momentum or the even smaller effects of the viscosity.

The second density flow experiment considers a high-density contrast problem. The densities of both fluids are 1000 and $1200\,\mathrm{kg/m^3}$. A rectangular basin with a length $L=48\,\mathrm{m}$ and a depth $H=16\,\mathrm{m}$ has initially a gate at $x=32\,\mathrm{m}$ that separates the two fluids (the heavy fluid being in the right side of the basin). A 96×32 mesh is used (both horizontal and vertical resolutions are 0.5 m) and the time step is 0.005 s. We let the fluid viscosity to be $\mu_x=\mu_z=0.45\,\mathrm{m^2/s}$, and the eddy dispersion coefficients for the salinity are $\nu_x=0.0001\,\mathrm{m^2/s}$ and $\nu_z=0\,\mathrm{m^2/s}$. In Figure 11, the salinity distribution is displayed at times $t=2, 4, 6, 8$ and 10 s. The velocity field is shown at time $t=6\,\mathrm{s}$ and the maximum velocity calculated by the model in the bottom layer is again nearly horizontal at 2.976 m/s in the left direction. The model maximum front velocity is displayed in Figure 12(a). In order to obtain a meaningful comparison, the velocity profile of the moving layer is again shown in Figure 12(b) and the numerically integrated mean front velocity is $-2.096\,\mathrm{m/s}$. Again, this value is found to be smaller than the predicted one, i.e. 2.697 m/s obtained from (43). The argument used above for the first experiment is still valid to explain the discrepancy between these two values.

DOI: 10.1002/fld

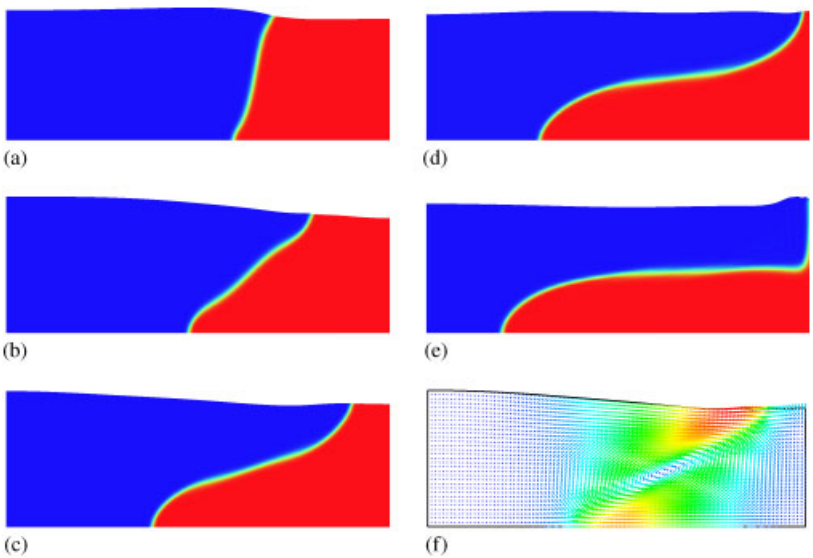

Figure 11. Computed salinity distribution for the high density contrast case at times: (a) 2 s; (b) 4 s; (c) 6 s; (d) 8 s; (e) 10 s; and (f) the velocity field at $t=6$ s where the minimum (blue) and maximum (red) values of u and w are $(-2.976, 3.610)$ and $(-1.432, 1.535)$, respectively.

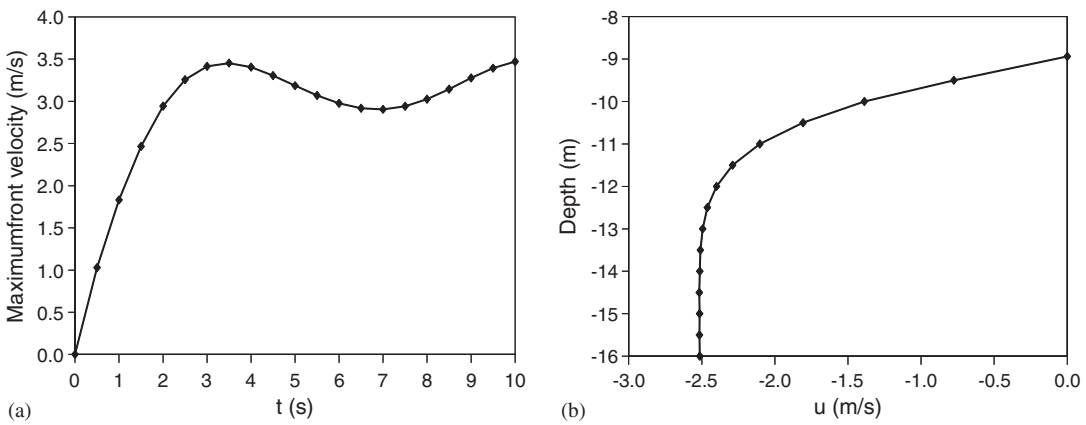

Figure 12. As for Figure 10 but at $t=6$ s.

7. CONCLUSION

In this paper, we have presented and validated a hydrodynamic model for two-dimensional vertical free-surface flows by using a fractional step algorithm. The non-hydrostatic Navier–Stokes equations are solved using the so-called P_1^{NC}–P_1 FE pair. The velocity and salinity fields are approximated by non-conforming linear FEs (P_1^{NC}), and both pressure and free-surface elevation are approximated by a linear continuous approximation (P_1). The most useful property of the P_1^{NC}

DOI: 10.1002/fld

basis functions is their orthogonality property, which considerably increases the computational efficiency of the model. Indeed, the P_1^{NC} mass matrix is diagonal leading to a tremendous saving in the computational cost and memory requirement.

Non-conforming FE schemes are well suited to advection-dominated flows. The inherent flexibility of the method permits to represent accurate solutions with steep gradients. Promising results have been obtained in [15] for a transport scalar equation using the P_1^{NC}–P_1 pair and in [16] for the propagation of the non-linear Rossby modes. In the present paper, the model is validated using three numerical tests, including a deepwater standing wave, the propagation of solitary wave in a long channel and the density-driven flow. The results are found in good agreement with the analytical solutions when they are available. These encouraging results suggest undertaking further extension towards a three-dimensional non-hydrostatic model with a realistic bathymetry. Further, we project to use the model to study the effect on thermal stratification of the three-dimensional flow near the water intake of hydropower plant. Such a case presents both the hydrostatic pressure in the reservoir and highly non-hydrostatic pressure near the intake with the combination of stratified flows in winter and summer regimes.

REFERENCES

1. Blumberg A, Mellor G. A description of a three-dimensional coastal ocean circulation model. In *Three-dimensional Coastal Ocean Models*, Mooers CNK (ed.). American Geophysical Union, 1987; 1–16.
2. Sheng YP. On modeling three-dimensional estuarine and marine hydrodynamics. In *Three-dimensional Models of Marine and Estuarine Dynamics*, Nihoul JC, Jamart BM (eds). Elsevier Oceanography Series. Elsevier: Amsterdam, 1987; 35–54.
3. Mamrick JM. A three-dimensional environmental fluid dynamic computer code: theoretical and computational aspects. *Special Report in Applied Marine Science and Ocean Engineering*, *No. 317*. Virginia Institute of Marine Science, College of Willian & Mary, Gloucester Point, VA, 1992.
4. Casulli V, Stelling G. Numerical simulation of 3D quasi-hydrostatic free-surface flows. *Journal of Hydraulic Engineering* 1998; **124**(7):678–686.
5. Casulli V. A semi-implicit finite difference method for non-hydrostatic free-surface flows. *International Journal for Numerical Methods in Fluids* 1999; **30**(4):425–440.
6. Mahadevan A, Oliger J, Street R. A nonhydrostatic mesoscale ocean model. Part II: numerical implementation. *Journal of Physical Oceanography* 1996; **26**(9):1881–1900.
7. Chen X. A fully hydrodynamic model for three-dimensional, free surface flows. *International Journal for Numerical Methods in Fluids* 2003; **42**(9):929–952.
8. Stelling G, Zijlema M. An accurate and efficient finite-difference algorithm for non-hydrostatic free-surface flow with application to wave propagation. *International Journal for Numerical Methods in Fluids* 2003; **43**(1):1–23.
9. Jankowski JA. A non-hydrostatic model for free surface flows. *Ph.D. Thesis*, University of Hannover, Hannover, 1998.
10. Huerta A, Liu W. Viscous flow with large free surface motion. *Computer Methods in Applied Mechanics and Engineering* 1988; **69**:277–324.
11. Ramaswamy B. Numerical simulation of unsteady viscous free surface flow. *Journal of computational Physics* 1990; **90**:396–430.
12. Hua BL, Thomasset F. A noise-free finite-element scheme for the two-layer shallow-water equations. *Tellus* 1984; **36A**:157–165.
13. Le Roux DY. Dispersion relation analysis of the P_1^{NC}–P_1 finite-element pair in shallow-water models. *SIAM Journal on Scientific Computing* 2005; **27**:394–414.
14. Le Roux DY, Rostand V, Pouliot B. Analysis of numerically-induced oscillations in 2D finite-element shallow-water models. Part I: inertia-gravity waves. *SIAM Journal on Scientific Computing* 2007; **29**:331–360.
15. Hanert E, Le Roux DY, Legat V, Deleersnijder E. Advection schemes for unstructured grid ocean modelling. *Ocean Modelling* 2004; **7**:39–58.
16. Hanert E, Le Roux DY, Legat V, Deleersnijder E. An efficient Eulerian finite-element method for the shallow-water equations. *Ocean Modelling* 2005; **10**:115–136.

DOI: 10.1002/fld

17. Chorin A. Numerical solution of the Navier–Stokes equations. *Mathematics of Computation* 1968; **22**:745–762.
18. Temam R. Une méthode d'approximation de la solution des équations de Navier–Stokes. *Bulletin de la Société Mathématique de France* 1968; **98**:115–152.
19. Gresho P. On the theory of semi-implicit projection methods for viscous incompressible flow and its implementation via a finite element method that also introduces a nearly consistent mass matrix. Part I: theory. *International Journal for Numerical Methods in Fluids* 1990; **11**:587–620.
20. Gresho P, Chan S. On the theory of semi-implicit projection methods for viscous incompressible flow and its implementation via a finite element method that also introduces a nearly consistent mass matrix. Part II: implementation. *International Journal for Numerical Methods in Fluids* 1990; **11**:587–620.
21. Hinton E, Rock T, Zienkiewicz OC. A note on mass lumping and related processes in the finite element method. *Earthquake Engineering and Structural Dynamics* 1976; **4**:245–249.
22. Fried I, Malkus DS. Finite element mass matrix lumping by numerical integration with no convergence rate loss. *International Journal of Solids and Structures* 1975; **11**:461–466.
23. Thomasset F. Implementation of finite element methods for Navier–Stokes equations. *Springer Series in Computational Physics*. Springer: Berlin, 1981.
24. UNESCO. Tenth report of the joint panel on oceanographic tables and standards. *UNESCO Technical Paper in Marine Science*, vol. 36, 1981; 25.
25. Le Méhauté B. *An Introduction to Hydrodynamics and Water Waves*. Springer: New York, 1976.
26. LeBlond P, Mysak L. Waves in the ocean. *Elsevier Oceanography Series*, vol. 20. Elsevier: Amsterdam, Oxford, New York, 1978.
27. Laitone E. The second approximation to cnoidal and solitary waves. *Journal of Fluid Mechanics* 1960; **9**:430–444.
28. van Rijn LC. *Principles of Fluid Flow and Surface Waves in Rivers*, *Estuaries*, *Seas and Oceans*. Aqua Publications: Amsterdam, 1994.

DOI: 10.1002/fld